2021 IEEE Conference on Control Technology and Applications (CCTA).
August 8-11, 2021. San Diego, California

2021 IEEE Conference on Control Technology and Applications (CCTA).
August 8-11, 2021. San

Optimal Shaping of the Safety Factor Profile in the EAST Tokamak*

Zibo Wang[1], Hexiang Wang[1], Eugenio Schuster[1], Zhengping Luo[2],
Yao Huang[2], Qiping Yuan[2], Bingjia Xiao[2], and David Humphreys[3]

2021 IEEE Conference on Control Technology and Applications (CCTA) | 978-1-6654-3643-4/21/$31.00 ©2021 IEEE | DOI: 10.1109/CCTA48906.2021.9658937

Abstract— **Tokamaks, which are one of the most promising approaches to energy generation from nuclear fusion, are toroidal devices confining a very hot ionized gas, i.e. plasma, where the nuclear reactions take place. Studies have shown that the shape of the safety-factor profile, which is related to the helical pitch of the magnetic fields used for plasma confinement, is a key factor towards achieving advanced operating conditions characterized by improved confinement, magnetohydrodynamic stability, and possible steady-state operation. In this work, a first-principles-driven, control-oriented model of the safety-factor profile evolution has been used to design linear-quadratic-integral (LQI) controllers for q-profile shaping in combination, in some cases, with plasma-energy regulation. Results based on nonlinear simulations are presented together with some initial experimental results from the EAST tokamak. A general framework for real-time control of both magnetic and kinetic plasma profiles and scalars has been implemented in the EAST Plasma Control System (PCS), enabling in this way the experimental testing of the proposed controllers. These experiments are among the first experiments on safety-factor profile control ever conducted on the EAST tokamak.**

I. Introduction

Nuclear fusion is a promising source of energy with the potential of effectively responding to the increasing world demand. It is achieved by fusing together two light nuclei, often isotopes of hydrogen like deuterium and tritium, to form one heavier nucleus. Because tremendous kinetic energy is required for the two nuclei to overcome the Coulomb repulsion force acting upon them, the fusion reaction can only take place by heating up the fuel to around 100 million degrees. At this high temperature, the fuel gas ionizes and becomes a plasma. During the fusion reaction, Δm of mass is converted into ΔE of energy release according to Einstein's mass-energy equivalence $\Delta E = \Delta m c^2$, where c is the speed of light in vacuum. In a deuterium-tritium fusion reaction, where an α particle (He_2^4 nuclei) and a neutron are produced, the released energy is 17.6 MeV per reaction. If 1 kg of this deuterium-tritium fuel were converted in energy, about 10^8 kWh of energy would be released. Fusion, as a source of essentially unlimited energy, has several advantages: no air pollution or greenhouse gases, no risk of nuclear accident, no generation of material for nuclear weapons, low-level radioactive waste, and a nearly infinite supply of fuel.

*This work was supported in part by the U.S. Department of Energy under contract DE-SC0010537.

[1]Z. Wang (zibo.wang@lehigh.edu), H. Wang and E. Schuster are with the Department of Mechanical Engineering and Mechanics, Lehigh University, Bethlehem, PA 18015, USA.

[2]Z. luo, Y. Huang, Q. Yuan and X. Xiao are with the Institute of Plasma Physics, Chinese Academy of Sciences, Hefei 230031, PRC.

[3]D. Humphreys is with General Atomics, San Diego, CA 92121, USA.

By exploiting the fact that both ions and electrons in the plasma respond to magnetic fields, tokamaks use strong magnetic fields to confine the hot plasma in a toroidal vacuum chamber. To make nuclear fusion a commercially viable means of producing energy, tokamak reactors must operate at high fusion gain (i.e., the power produced from the reactor must be greater than the power required to sustain the plasma conditions needed for nuclear fusion) for extended periods of time, and ideally reaching steady-state operation. The key to achieving stable and steady-state operation in high fusion-gain plasmas is linked to the ability to control the spatial distribution of critical plasma properties such as the electron density n_e, electron temperature T_e, ion temperature T_i, and safety factor q, which is a measure of the helical pitch of the magnetic fields (as shown in Figure 1) used for confining the hot plasma. The one-dimensional spatial shape of these plasma properties is usually referred to as profile. In particular, the ability to shape the q profile is essential for avoiding magnetohydrodynamic (MHD) instabilities, improving confinement, and achieving steady-state operation. The plasma profiles can be shaped by available plasma actuators, which may act on the interior of the plasma (typically auxiliary heating, current drive, particle injection) or at the boundary of the plasma (inductive voltage from the primary Ohmic transformer, gas flux, particle recycling).

Recently, several control algorithms for q-profile regulation have been proposed by following robust-control [1], [2], [3], [4], model-predictive-control [5], [6] and optimal-control [7], [8], [9] approaches. While focused on the EAST tokamak in China, this work differentiates itself from [3], [4], [6] by following a linear-quadratic-integral (LQI) control approach and presenting for the first time experimental results on model-based q-profile regulation in EAST. The design is based on a first-principles-driven (FPD), control-oriented model of the safety factor dynamics [10], [11], which is governed by a one-dimensional partial differential equation (PDE) referred to as the magnetic diffusion equation (MDE), in combination with a zero-dimensional power balance equation. A finite-difference method is employed to reduce the order of the MDE. Moreover, approximate linearization is used to further simplify the obtained ordinary differential equation (ODE) system. The model, which captures the linearized dynamics of the q-profile, is finally used for the design of linear-quadratic-integral (LQI) controllers. The performances of these controllers are assessed in nonlinear simulations before experimental testing. The q-profile controllers can be implemented in a newly created Profile Control category within the EAST Plasma Control System

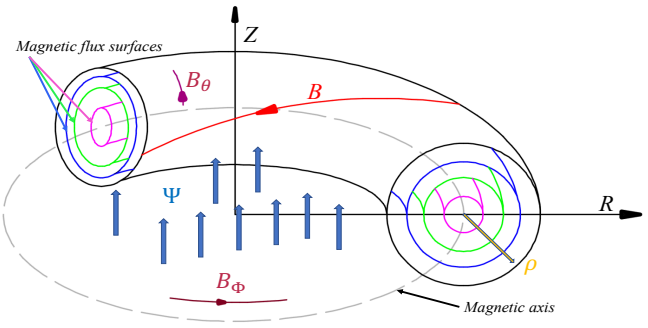

Fig. 1. Magnetic configuration in a tokamak. The poloidal (B_θ) and toroidal (B_Φ) magnetic fields combine to produce a helical magnetic field B, which confines the plasma. In the poloidal plane, which is defined by the radial and vertical axes with coordinates R and Z, respectively, each point is characterized by a value of the poloidal magnetic flux $\Psi(R,Z)$. Points with identical $\Psi(R,Z)$ values define nested magnetic flux surfaces around a magnetic axis. Any quantity indexing these magnetic flux surfaces from the magnetic axis to the boundary could be adopted as spatial coordinate ρ.

(PCS). The q-profile is computed in real time from magnetic measures in EAST via the equilibrium reconstruction algorithm p-EFIT [12]. The total plasma current, together with the powers of different current drives, are commanded from the Profile Control category to regulate the q-profile.

This paper is organized as follows. The response models for the q-profile and plasma stored energy are introduced in Section II. Details on model reduction and control design are provided in Section III. Simulation results for several control objectives are presented in Section IV. Initial experimental results from EAST illustrating the effectiveness of the proposed controller to regulate the q-profile in the core and at the edge of the plasma is presented in Section V. Conclusions and plans for future work are stated in Section VI.

II. Poloidal Magnetic Flux and Energy Evolution Models

As shown in Fig. 1, the helical magnetic field confining the plasma inside the tokamak can be written as $\bar{B}=\bar{B}_\phi+\bar{B}_\theta$, where $\bar{B}_\phi$ denotes the toroidal magnetic flux and $\bar{B}_\theta$ denotes the poloidal magnetic flux. The poloidal magnetic flux at a point P on the poloidal plane, defined by the Z and R axes, is defined as $\Psi \triangleq \int_S \bar{B}_\theta \cdot d\bar{S}$, where $\bar{B}_\theta$ is the poloidal component of the magnetic field, and S is the surface whose boundary is a toroidal ring that passes through P and is normal to the Z axis. Under ideal MHD equilibrium conditions [13], the magnetic-flux surfaces in a tokamak form toroidally nested surfaces around the magnetic axis (see Fig. 1). The magnetic-flux surfaces can be labeled by a single coordinate within the R-Z plane. This fact, together with the assumption of toroidal symmetry, reduce the 3D-problem in space to a 1D-problem. In this work, the spatial coordinate is chosen as the mean effective minor radius, $\rho \triangleq \sqrt{\Phi/(B_{\phi,0}\pi)}$, where $B_{\phi,0}$ is the vacuum toroidal magnetic field at the major radius, R_0. The toroidal magnetic flux, Φ, is defined as $\Phi \triangleq \int_{S_\phi} \bar{B}_\phi \cdot d\bar{S}_\phi$, where S_ϕ is the surface whose boundary is the magnetic-flux surface defined by P and is normal to the ϕ axis. A normalized version of ρ is given by $\hat{\rho} \triangleq \rho/\rho_b$, where ρ_b is the mean effective minor radius of the last-closed magnetic-flux surface, also known as the plasma boundary.

The safety factor, q, is defined as

$$q(\hat{\rho},t) = -\frac{d\Phi}{d\Psi} = -\frac{d\Phi/d\rho}{d\Psi/d\rho} = -\frac{B_{\phi,0}\rho_b^2\hat{\rho}}{\partial\psi/\partial\hat{\rho}}, \tag{1}$$

where $\psi \triangleq \Psi/(2\pi)$ is the poloidal stream function. It is clear from (1) that the dynamics of q is determined by the dynamics of ψ.

A. Poloidal Magnetic Flux Dynamics

The evolution of the poloidal magnetic flux (ψ) is governed by the magnetic diffusion equation (MDE) [14],

$$\frac{\partial\psi}{\partial t} = \frac{\eta(T_e)}{\mu_0\rho_b^2\hat{F}^2}\frac{1}{\hat{\rho}}\frac{\partial}{\partial\hat{\rho}}\left(\hat{\rho}D_\psi\frac{\partial\psi}{\partial\hat{\rho}}\right) + R_0\hat{H}\eta(T_e)\frac{\langle\bar{j}_{NI}\cdot\bar{B}\rangle}{B_{\phi,0}}, \tag{2}$$

with two given boundary conditions,

$$\left.\frac{\partial\psi}{\partial\hat{\rho}}\right|_{\hat{\rho}=0} = 0, \quad \left.\frac{\partial\psi}{\partial\hat{\rho}}\right|_{\hat{\rho}=1} = \frac{k}{2}I_p(t), \quad k = -\frac{\mu_0}{\pi}\frac{R_0}{\hat{G}(1)\hat{H}(1)}, \tag{3}$$

where $\hat{F}(\hat{\rho})$, $\hat{G}(\hat{\rho})$, $\hat{H}(\hat{\rho})$ and $D_\psi(\hat{\rho}) = \hat{F}(\hat{\rho})\hat{H}(\hat{\rho})\hat{G}(\hat{\rho})$ are spatially varying geometric factors pertaining to the magnetic configuration of a particular plasma equilibrium, I_p is the plasma current, μ_0 is the vacuum permeability, and $\langle\cdot\rangle$ denotes a flux-surface average. Control-oriented models for the electron temperature and density (T_e and n_e), ion temperature and density (T_i and n_i), plasma resistivity η, and non-inductive current-drive $\frac{\langle\bar{j}_{NI}\cdot\bar{B}\rangle}{B_{\phi,0}}$ are needed for closure of the MDE [10], [11]. It is worth noting that the boundary condition at $\hat{\rho}=1$ is actually evaluated near the flux surface.

A tight coupling between the electron and ion species in the plasma is assumed. This implies that electron and ion densities and temperatures are treated as identical (i.e., $n_e \approx n_i$ and $T_e \approx T_i$). The electron density $n_e(\hat{\rho},t)$ is modeled as

$$n_e(\hat{\rho},t) = n_e^{prof}(\hat{\rho})\bar{n}_e(t), \tag{4}$$

where n_e^{prof} is a reference electron density profile and $\bar{n}_e(t)$ is the line-averaged electron density.

The electron temperature is modeled as

$$T_e(\hat{\rho},t) = T_e^{prof}(\hat{\rho})I_p(t)^\alpha P_{tot}(t)^\gamma \bar{n}_e(t)^\kappa, \tag{5}$$

where T_e^{prof} is a reference electron temperature profile and α, γ, κ are positive scaling factors.

The plasma resistivity $\eta(T_e)$ scales with the electron temperature as

$$\eta(\hat{\rho},t) = \frac{k_{sp}(\hat{\rho})Z_{eff}}{T_e(\hat{\rho},t)^{3/2}}, \tag{6}$$

where k_{sp} is a constant and Z_{eff} is the effective atomic number of the ion species in the plasma.

The non-inductive current drive (j_{NI}) is the sum of the self-generated bootstrap current (j_{BS}) and each of the auxiliary sources such as lower hybrid wave current drive (j_{LHW}) and neutral beam injection (j_{NBI}),

$$\frac{\langle\bar{j}_{NI}\cdot\bar{B}\rangle}{B_{\phi,0}} = \sum_{i=1}^{4}\frac{\langle\bar{j}_{NBI_i}\cdot\bar{B}\rangle}{B_{\phi,0}} + \sum_{i=1}^{2}\frac{\langle\bar{j}_{LHW_i}\cdot\bar{B}\rangle}{B_{\phi,0}} + \frac{\langle\bar{j}_{BS}\cdot\bar{B}\rangle}{B_{\phi,0}}. \tag{7}$$

In this work, we consider six of EAST's non-inductive current sources, namely four neutral beam injection (NBI) and two lower hybrid wave (LHW) current-drive sources. Each auxiliary source $\frac{\langle \bar{j}_x \cdot \bar{B} \rangle}{B_{\phi,0}}$, where $x \in \{NBI_i, LHW_i\}$, is modeled in this work by the product of a reference deposition profile $j_i^{dep}(\hat{\rho})$, an efficiency term $\frac{T_e(\hat{\rho},t)^{\delta}}{n_e(\hat{\rho},t)}$ where δ is 0.5 for NBI and 1 for LHW, and the power associated with the source $P_x(t)$, i.e.

$$\frac{\langle \bar{j}_x \cdot \bar{B} \rangle}{B_{\phi,0}}(\hat{\rho},t) = j_x^{dep}(\hat{\rho}) \frac{T_e(\hat{\rho},t)^{\delta}}{n_e(\hat{\rho},t)} P_x(t). \tag{8}$$

The bootstrap current model is based on [15], which after incorporating the electron-ion tight coupling assumption reduces to

$$\frac{\langle \bar{j}_{BS} \cdot \bar{B} \rangle}{B_{\phi,0}}(\hat{\rho},t) = \frac{R_0}{\hat{F}} \left(\frac{\partial \psi}{\partial \hat{\rho}} \right)^{-1} [\mathscr{L}_1 T_e \frac{\partial n_e}{\partial \hat{\rho}} + \mathscr{L}_2 n_e \frac{\partial T_e}{\partial \hat{\rho}}], \tag{9}$$

where the spatial functions $\mathscr{L}_1(\hat{\rho})$ and $\mathscr{L}_2(\hat{\rho})$ depend on the magnetic configuration of a particular plasma equilibrium.

With all the control-oriented models introduced above, the MDE (2) can be rewritten as

$$\frac{\partial \psi}{\partial t} = \left(C_{f_1} \frac{\partial \psi}{\partial \hat{\rho}} + C_{f_2} \frac{\partial^2 \psi}{\partial \hat{\rho}^2} \right) u_{diff} + \sum_i C_{j_i} u_{j_i} + C_{j_{bs}} \left(\frac{\partial \psi}{\partial \hat{\rho}} \right)^{-1} u_{j_{bs}}. \tag{10}$$

By differentiating (10) with respect to $\hat{\rho}$, the MDE is rewritten in terms of the gradient of the poloidal magnetic flux ($\theta = \partial \psi / \partial \hat{\rho}$) as

$$\begin{aligned} \frac{\partial \theta}{\partial t} = & \left[\frac{dC_{f_1}}{d\hat{\rho}} \theta + \left(C_{f_1} + \frac{dC_{f_2}}{d\hat{\rho}} \right) \frac{\partial \theta}{\partial \hat{\rho}} + C_{f_2} \frac{\partial^2 \theta}{\partial \hat{\rho}^2} \right] u_{diff} + \\ & \sum_i \frac{dC_{j_i}}{d\hat{\rho}} u_{j_i} + \frac{dC_{j_{bs}}}{d\hat{\rho}} \frac{1}{\theta} u_{j_{bs}} - C_{j_{bs}} \frac{1}{\theta^2} \frac{\partial \theta}{\partial \hat{\rho}} u_{j_{bs}} \triangleq f_{\theta}, \end{aligned} \tag{11}$$

$$i \in [nbi_1, \cdots, nbi_{n_{nbi}}, lhw_1, \cdots, lhw_{n_{lhw}}].$$

where

$$C_{f_1}(\hat{\rho}) = \frac{k_{sp}(\hat{\rho}) Z_{eff} \mu_0^{-1} \rho_b^{-2}}{\hat{F}^2 \overline{T}_e^{prof}(\hat{\rho})^{1.5}} \left(\frac{D_{\psi}}{\hat{\rho}} + \frac{dD_{\psi}}{d\hat{\rho}} \right), \tag{12}$$

$$C_{f_2}(\hat{\rho}) = \frac{k_{sp}(\hat{\rho}) Z_{eff} \mu_0^{-1} \rho_b^{-2}}{\hat{F}^2 \overline{T}_e^{prof}(\hat{\rho})^{1.5}} D_{\psi}, \tag{13}$$

$$u_{diff}(t) = \sqrt{I_p(t)^{-3\gamma} P_{tot}(t)^{-3\varepsilon} \bar{n}_e(t)^{-3\zeta}}, \tag{14}$$

$$C_{j_i}(\hat{\rho}) = \frac{R_0 \hat{H} k_{sp}(\hat{\rho}) Z_{eff} k_i(\hat{\rho}) j_i^{dep}(\hat{\rho})}{\overline{T}_e^{prof}(\hat{\rho})^{(1.5-\delta)} n_e^{prof}(\hat{\rho})}, \tag{15}$$

$$u_{j_i}(t) = (I_p(t)^{\gamma} P_{tot}(t)^{\varepsilon})^{(\delta-1.5)} \bar{n}_e(t)^{(\zeta(\delta-1.5)-1)} P_i(t), \tag{16}$$

$$C_{j_{bs}}(\hat{\rho}) = \frac{R_0^2 \hat{H} k_{sp}(\hat{\rho})}{\hat{F} Z_{eff}^{-1}} \left[\frac{\mathscr{L}_1(\hat{\rho}) dn_e^{prof}(\hat{\rho})/d\hat{\rho}}{\overline{T}_e^{prof}(\hat{\rho})^{0.5}} + \right. \tag{17}$$

$$\left. \frac{\mathscr{L}_2(\hat{\rho}) n_e^{prof}(\hat{\rho}) d(\overline{T}_e^{prof}(\hat{\rho}))/d\hat{\rho}}{\overline{T}_e^{prof}(\hat{\rho})^{1.5}} \right], \tag{18}$$

$$u_{j_{bs}}(t) = I_p(t)^{-0.5\gamma} P_{tot}(t)^{-0.5\varepsilon} \bar{n}_e(t)^{1-0.5\zeta}. \tag{19}$$

The boundary conditions in (3) becomes

$$\theta(0,t) = 0, \qquad \theta(1,t) = \frac{k_{I_p}}{2} I_p(t). \tag{20}$$

The plasma inductance is an integral function of q, and therefore of θ. It is usually employed as a measure of the q-profile broadness or peakedness, and it is defined as

$$l_i = \frac{8\pi^2}{\mu_o {}^2 R_o {}^2 I_p {}^2} \int_0^1 \hat{\rho} \hat{G} \hat{H} \theta^2 d\hat{\rho}. \tag{21}$$

B. Plasma Stored Energy Dynamics

The evolution of the plasma stored energy density averaged over the plasma volume can be approximately modeled by the nonlinear first-order equation

$$\frac{dW}{dt} = -\frac{W}{\tau_E(t)} + P_{tot}(t) \triangleq f_W, \tag{22}$$

where τ_E is the global energy confinement time.

$$\tau_E \propto I_p(t)^{\alpha} P_{tot}(t)^{(\gamma-1)} \bar{n}_e(t)^{(1+\kappa)}. \tag{23}$$

The model used in this work for τ_E is based on the $IPB98(y,2)$ scaling law [16], which results in $\alpha = 0.96$, $\gamma = 0.27$, and $\kappa = -0.6$. The total injected power is defined as $P_{tot} = P_{aux} + P_{ohm} - P_{rad}$, where P_{aux} is the total auxiliary heating/current-drive (H&CD) power, P_{ohm} is the Ohmic power, and P_{rad} is the radiation power.

The normalized plasma beta, β_N, is a measure of the ration between the kinetic energy in the plasma and the magnetic energy used for confinement. It is related to the plasma stored energy W through

$$\beta_N = \frac{(2/3)W/V_p}{B_{\phi,0}{}^2/(2\mu_0)} \frac{aB_{\phi,0}}{I_p}, \tag{24}$$

where a is the minor radius of the plasma, and V_p is the plasma volume.

III. Model Reduction and Controller Design

A. Model Reduction via Finite Difference

The infinite-dimensional model, described by the PDE shown in (11), can be reduced by discretizing the spatial domain on a uniform grid. The uniform grid is defined as

$$\Delta\hat{\rho} = \frac{1}{n-1}, \quad \hat{\rho}_i = (i-1) \cdot \Delta\hat{\rho}, \quad i \in \{1, \cdots, n\}. \tag{25}$$

The variable θ at $\hat{\rho}_i$ can be represented as $\theta_i = \theta(\hat{\rho}_i, t)$. Over the interior nodes $(\hat{\rho}_2, \cdots, \hat{\rho}_{n-1})$, the spatial derivatives of θ are approximated by a second-order Taylor series expansion to obtain

$$\left. \frac{\partial \theta}{\partial \hat{\rho}} \right|_i \approx \frac{\theta_{i+1} - \theta_{i-1}}{2\Delta\hat{\rho}}, \quad \left. \frac{\partial^2 \theta}{\partial \hat{\rho}^2} \right|_i \approx \frac{\theta_{i+1} - 2\theta_i + \theta_{i-1}}{(\Delta\hat{\rho})^2}. \tag{26}$$

By defining $Z = [\theta_2, \cdots, \theta_{n-1}, w]$, and $F = [f_{\theta}, f_W]$, the discretized dynamic model combining (11) and (22) is written as

$$\dot{Z} = F(Z, u), \tag{27}$$

with $u = [u_{diff}, u_{j_{bs}}, u_{j_{nbi_1}}, \cdots, u_{j_{nbi_{n_{nbi}}}}, u_{j_{lhw_1}}, \cdots, u_{j_{lhw_{n_{lh}}}}, I_p]^T$.

B. Linearization of Error Model

In order to design an LQI controller, the dynamic model (27) is linearized around a given reference trajectory (Z_{ref}, u_{ref}) by using a first-order Taylor series expansion

$$\dot{Z} \approx F(Z_{ref}, u_{ref}) + \left.\frac{\partial F}{\partial Z}\right|_{(Z_{ref},u_{ref})} (Z - Z_{ref}) + \left.\frac{\partial F}{\partial u}\right|_{(Z_{ref},u_{ref})} (u - u_{ref}). \quad (28)$$

By recalling that $\dot{Z}_{ref} = F(Z_{ref}, u_{ref})$ and defining $\Delta_Z \triangleq Z - Z_{ref}$, $\Delta_u \triangleq u - u_{ref}$, model (28) becomes

$$\dot{\Delta_Z} = A\Delta_Z + B\Delta_u, \quad (29)$$

where the Jacobian matrices A and B are given by

$$A \triangleq \left.\frac{\partial F}{\partial Z}\right|_{(Z_{ref},u_{ref})}, \quad B \triangleq \left.\frac{\partial F}{\partial u}\right|_{(Z_{ref},u_{ref})}. \quad (30)$$

C. Linear Quadratic Integral (LQI) Control Design

The control objective could be to regulate the system around the reference trajectory with minimum change of the plasma current and H&CD power. A linear-quadratic-regulator (LQR) could be used in this case to find the optimal solution (ie., to minimize the control effort Δ_u while minimizing Δ_Z subject to the dynamic constraints imposed by the model (29). A more general control objective could be, however, to track a desired output trajectory.

For instance, the outputs to be tracked could be the deviations with respect to the reference values of the q-profile profile at specific locations, the normalized beta β_N, or the internal inductance l_i. The relationship between q and θ is given by (1). By using a Taylor series expansion around the reference trajectory and neglecting higher-order terms, the deviation from the reference value can be expressed as

$$\Delta_q = \left.\frac{B_{\phi,0}{\rho_b}^2 \hat{\rho}}{\theta^2}\right|_{\theta=\theta^{ref}} \Delta_\theta, \quad (31)$$

where $\Delta_q = q - q_{ref}$ and $\Delta_\theta = \theta - \theta_{ref}$. By following a similar approach, the deviation from β_N from its reference value can be expressed from (24) as

$$\begin{aligned} \Delta\beta_N &= \left.\frac{(2/3)/V_p}{{B_{\phi,0}}^2/(2\mu_0)} \frac{aB_{\phi,0}}{I_p}\right|_{I_p=I_p^{ref}} \Delta W \\ &- \left.\frac{(2/3)W/V_p}{{B_{\phi,0}}^2/(2\mu_0)} \frac{aB_{\phi,0}}{{I_p}^2}\right|_{I_p=I_p^{ref},W=W^{ref}} \Delta I_p, \end{aligned} \quad (32)$$

and the deviation of l_i from its reference value can be obtained from (21) as

$$\begin{aligned} \Delta l_i &= \frac{16\pi^2\Delta\rho}{{\mu_o}^2{R_o}^2} \begin{bmatrix} \frac{\hat{G}\hat{H}\hat{\rho}(2)\theta^{ref}(2)}{{I_p^{ref}}^2} \\ \frac{\hat{G}\hat{H}\hat{\rho}(3)\theta^{ref}(3)}{{I_p^{ref}}^2} \\ \vdots \\ \frac{\hat{G}\hat{H}\hat{\rho}(n-1)\theta^{ref}(n-1)}{{I_p^{ref}}^2} \end{bmatrix}^T \Delta\theta \\ &- \frac{16\pi^2\Delta\rho}{{\mu_o}^2{R_o}^2} \left(\sum_{i=2}^{n-1} \frac{\hat{G}\hat{H}\hat{\rho}(i)\theta^{ref}(n-1)^2}{{I_p^{ref}}^3}\right)\Delta I_p \end{aligned} \quad (33)$$

Finally, by defining the output as a combination of Δq (31) at specific locations, $\Delta\beta_N$ (32), and Δl_i (33), the output equation can always be written as

$$\Delta_y = C\Delta_Z + D\Delta_u. \quad (34)$$

By assuming that the output trajectory to be tracked is feasible, i.e. it satisfies (29) and (34),

$$\dot{\Delta_Z^d} = A\Delta_Z^d + B\Delta_u^d, \quad \Delta_y^d = C\Delta_Z^d + D\Delta_u^d, \quad (35)$$

the dynamics of the tracking-error state $\Delta_Z^e \triangleq \Delta_Z - \Delta_Z^d$ and output $\Delta_y^e \triangleq \Delta_y - \Delta_y^d$ will be subject to the same constraints with input $\Delta_u^e \triangleq \Delta_u - \Delta_u^d$. The LQR control problem could be stated then for the tracking-error system. To include integral action, the state is augmented with the time integral of Δ_y^e,

$$\bar{x} \triangleq [(\Delta_Z^e)^T, \int_0^t (\Delta_y^e)^T dt]^T. \quad (36)$$

Then, the optimal control problem is stated as

$$\min_K \int_{t_0}^{\infty} (\bar{x}^T Q\bar{x} + (\Delta_u^e)^T R\Delta_u^e) dt \quad (37)$$

$$\text{subject to} \quad \dot{\bar{x}} = \overline{A}\bar{x} + \overline{B}\Delta_u^e, \quad (38)$$

$$\Delta_u^e = -K\bar{x}, \quad (39)$$

where $Q = diag([\mathbf{0}, w_1, \ldots, w_k]) \in \mathbb{R}^{(n-1+k)\times(n-1+k)}$ (k is the dimension of the vector Δ_y^e) and $R \in \mathbb{R}^{m\times m}$ (m is the dimension of the vector Δ_u^e) are positive semidefinite and positive definite weighting matrices, and

$$\overline{A} = \begin{bmatrix} A & \mathbf{0} \\ C & \mathbf{0} \end{bmatrix}, \quad \overline{B} = \begin{bmatrix} B \\ D \end{bmatrix}. \quad (40)$$

The solution of (37)–(39) is obtained by solving the well-known associated Riccati Algebraic Equation (ARE) [17].

IV. Simulation Testing of LQI

The proposed LQI is tested in nonlinear simulations based on the FPD, control-oriented models of the poloidal magnetic flux and plasma stored energy described in Section II. The target q-profile and stored-energy evolutions are obtained by executing feedforward-only simulations to make sure that they are reachable targets. Then, the capability of the LQI controllers to track the target evolutions are determined by running feedforward + feedback simulations with feedforward inputs and initial conditions that are different from those used for target generation. Four different cases are illustrated in this section as a function of the controlled variables: Case 1: $q(0.1)$, $q(0.9)$, Case 2: $q(0.1)$, $q(0.5)$, $q(0.9)$ Case 3: $q(0.1)$, $q(0.9)$, β_N, Case 4: l_i, $q(0.9)$, β_N. I_p, P_{LH1} and P_{LH2} are used as actuators for all cases with the exemption of Case 1, where only I_p and P_{LH2} are used as actuators. The feedback controller is turned on at 2 seconds in all the feedforward + feedback simulation studies.

Figures 2 compare both feedforward-only (FF) and feedforward + feedback (FF+FB) evolutions as predicted by the infinite-dimensional nonlinear FPD model with the desired targets. In Case 1, two spatial points of the q-profile are controlled as denoted by the blue dash-dotted lines in Figure 2 (a) and (c). In Case 2, three spatial points of the q-profile

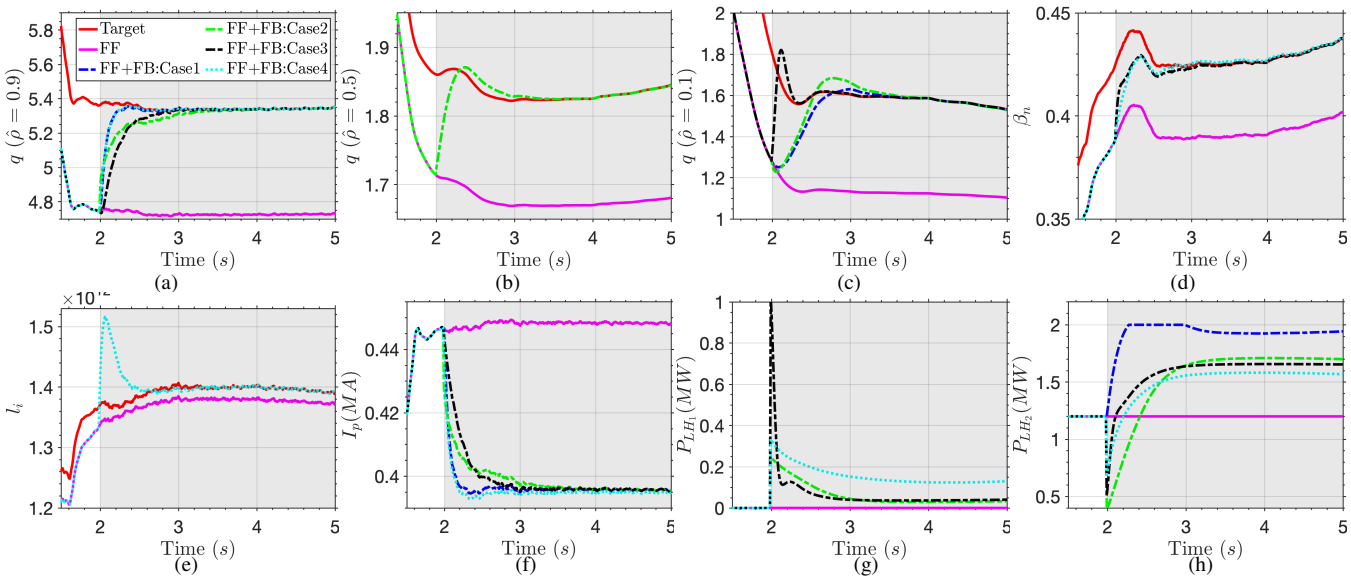

Fig. 2. Simulation testing of LQI controllers. Time evolutions of feedforward-only, feedforward + feedback controlled, and target q-profile at three points in space: (a) $\hat{\rho} = 0.9$, (b) $\hat{\rho} = 0.5$, and (c) $\hat{\rho} = 0.1$. Time evolutions of target, feedforward-only, and feedforward + feedback controlled scalars: (d) β_N, (e) l_i. Time evolutions of actuators ((f) I_p, (g) 2.45 GHz lower hybrid power, and (h) 4.60 GHz lower hybrid power) are plotted both for FF-only and FF+FB simulations. White region: feedback off; shadow region: feedback on.

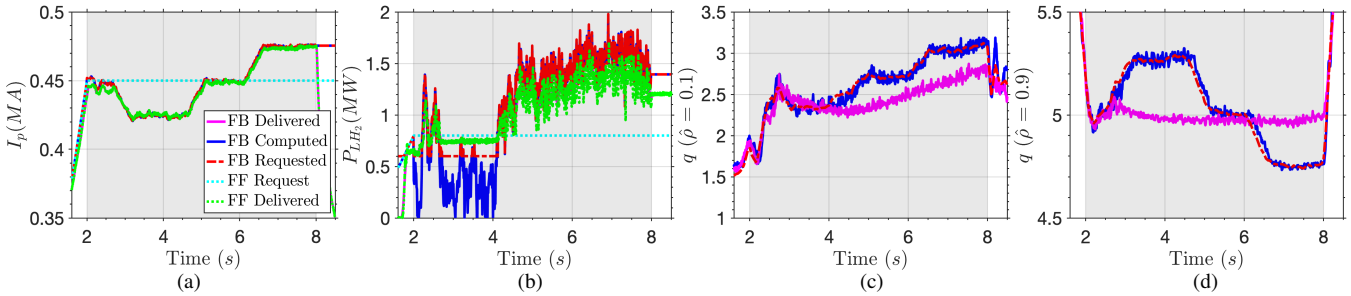

Fig. 3. Time evolutions of actuators ((a) plasma current, (b) 4.60 GHz LHW power) are shown both for FF-only and FF+FB experimental runs. Time evolutions of the feedforward-only, feedforward + feedback controlled, and target q-profile at two points in space: (c) $\hat{\rho} = 0.1$, (d) $\hat{\rho} = 0.9$. White region: feedback off; shadow region: feedback on.

are controlled as denoted by the green dash-dotted lines in Figure 2 (a)-(c). In Case 3, two spatial points of the q-profile and β_N are controlled as denoted by the black dash-dotted lines in Figure 2 (a), (c) and (d). In Case 4, one spatial point of the q-profile and both β_N and l_i are controlled as denoted by the cyan dotted lines in Figure 2 (a), (d) and (e). The control inputs (I_p and P_{LH2}) corresponding to FF+FB simulations for Case 1 (blue dash-dotted lines) are shown as functions of time in Figure 2 (f)-(h). The control inputs (I_p P_{LH1} and P_{LH2}) corresponding to FF+FB simulations for Case 2 (green dash-dotted lines), Case 3 (black dash-dotted lines), and Case 4 (cyan dotted line) are shown as functions of time in Figure 2 (f)-(g). The FF simulation is denoted by the magenta lines in all the figures.

Although the dynamic evolution of the q-profile is nonlinearly coupled with several plasma parameters and controlled inputs, the q-profile at the edge is mainly affected by I_p, while the q-profile at the core is impacted by LHW sources. As it can be noted from the blue dash-dotted lines in Figure 2 (f) and (g), the actuators respond immediately once the controller is turned on. The q-profile targets both at the edge and in the core are greater than the feedforward trajectories. Therefore, the feedback controller drives I_p to a lower value and P_{LH_2} to a higher value in its effort to reach the targets. Because the maximum LHW power in this simulation is 2 MW, P_{LH_2} saturates between 2.2-3.2 second, which makes the tracking of $q(\hat{\rho} = 0.1)$ not that accurate in that time slot. The tracking of $q(\hat{\rho} = 0.9)$ is better because saturation is avoided. It is worth mentioning that the rate of change of I_p is set to be slow (i.e., a rate limit is imposed). Otherwise, I_p would probably fluctuate, which could cause a plasma disruption. On the other hand, the modulation of P_{LH_2} can be more aggressive. This can be appreciated in the green dash-dotted lines in Figure 2 (g) and (h), where P_{LH_1} jumps to 0.25 MW from zero and P_{LH_2} drops to 0.46 MW from 1.2 MW once the controller is turned on. These abrupt changes are indeed physically feasible. Because the rate of change for I_p in Case 2 is set slower than in Case 1 as shown in Figure 2 (f) (i.e., the green and blue dash-dotted lines), it takes more time to drive $q(\hat{\rho} = 0.9)$ to the desired target. It can be appreciated from the green dash-dotted lines in Figure 2 (b) and (c) that q at the other two points slightly overshoot and then successfully match the desired targets. In Case 3, the q-profile in the plasma core (black dash-dotted

line in Figure 2 (c)) is driven to its target very fast although the quick change of LHW power (dash-dotted line in black in Figure 2 (g)) causes an overshoot at beginning. As shown in dash-dotted line in black in Figure 2 (a) and (d), $q(\hat{\rho}=0.9)$ and β_n reach their target values almost at the same time. This is due to the high coupling between them; β_n is related to both I_p and the plasma stored energy (which mainly depends on the LHW power). In Case 4, two scalars and the q-profile at the edge are simultaneously controlled as shown in the cyan dotted line in Figure 2 (a), (c) and (e). As it can be noted from the cyan dotted line in Figure 2 (e), l_i has a large overshoot. This is because of its dependence on both $q(\hat{\rho}=0.9)$ and β_n, which need to also be driven higher. Figure 2 show that during the time interval $t \in [2,5]$ s the LQI controllers are capable of controlling both points of q and key scalar plasma properties (β_n and l_i) by steering the plasma actuators through feedback action.

V. Experimental Testing of LQI controller

The controller designed in Case 1 has been implemented in the EAST PCS and tested in reference-tracking and disturbance-rejection experiments. To keep the operation in H-mode, Electron Cyclotron Range of Frequency (ECRF) heating was used during the experiment. First, a reference shot (#95176) was obtained by executing a feedforward-only experiment where the ohmic coils and the high-frequency (4.6GHz) LHW source were used as actuators (I_p and P_{LH2}). By modifying the power of the LHW source in a second feedforward-only shot, a feasible q-profile evolution was obtained. This evolution was used as target in a feedforward+feedback shot (#95181) where the actuator trajectories of the reference shot were used as feedforward inputs.

The comparison between the feedforward-only shot (#95176) and the feedforward+feedback shot (#95181) is shown in Figure 3, where the q-profile tracking results are shown in Fig. 3(c)-(d), and the I_p and P_{LH2} actuations are shown in Fig. 3(a) and Fig. 3(b), respectively. When feedback control is turned on in shot #95181 during the time interval $t \in [2,8]$ s, the feedforward-only actuation is corrected by the quick reaction of total plasma current and the high-frequency LHW source power (as shown in Fig. 3(a)-(b)) to decrease the q-profile tracking errors both in the plasma core and near the plasma boundary. The initial disturbance introduced by suddenly turning on feedback control is effectively handled by the controller, and the q-profile target is successfully tracked as shown in Fig. 3(c)-(d) in spite of P_{LH2} saturating at its minimum level during the interval $t \in [2,4]$ s.

VI. Conclusions and Future Work

In this work, a well-known optimal control technique is successfully applied to one of the most challenging problems in fusion-plasma control, i.e. the control of the q-profile. A model composed by a PDE describing the dynamics of the q-profile evolution and an ODE describing the dynamics of the plasma stored energy is employed for the design of an LQI controller for the EAST tokamak. After model reduction and approximate linearization, the control problem is finally stated as an optimization problem where a cost function weighing both the control effort and the tracking error is minimized subject to the linearized dynamic model. The resulting feedback controller, which incorporates integral action, is proved to be effective at tracking a desired trajectory. A nonlinear simulation study for four different control objectives shows the potential of the proposed control algorithm to control a combination of the q-profile, β_N, and l_i. Initial experimental testing of the simplest of the four different controllers shows promising results. Ongoing and future work includes further experimental testing of these controllers by increasing the number of physical actuators connected to the Profile Control category in the EAST PCS.

References

[1] J. Barton, M. Boyer, W. Shi and E. Schuster, "Toroidal current profile control during low confinement mode plasma discharges in DIII-D via first-principles-driven model-based robust control synthesis," *Nucl. Fusion*, vol. 52, p. 123018, 2012.

[2] J. Barton, K. Besseghir, J. Lister, and E. Schuster, "Physics-based control-oriented modeling and robust feedback control of the plasma safety factor profile and stored energy dynamics in ITER," *Plasma Physics and Controlled Fusion*, vol. 57, no. 11, p. 115003, 2015.

[3] H. Wang and E. Schuster, "Robust control of the current profile and plasma energy in EAST," *Fusion Engineering and Design*, vol. 146, pp. 688–691, 2019.

[4] S. Wang, E. Witrant, and D. Moreau, "Robust control of q-profile and βp using data-driven models on EAST," *Fusion Engineering and Design*, vol. 162, p. 112071, 2021.

[5] E. Maljaars, F. Felici, T. Blanken, C. Galperti, O. Sauter, M. De Baar, F. Carpanese, T. Goodman, D. Kim, S. Kim, *et al.*, "Profile control simulations and experiments on TCV: a controller test environment and results using a model-based predictive controller," *Nuclear Fusion*, vol. 57, no. 12, p. 126063, 2017.

[6] H. Wang, W. P. Wehner, and E. Schuster, "Combined current profile and plasma energy control via model predictive control in the EAST tokamak," in *2018 26th Mediterranean Conference on Control and Automation (MED)*. IEEE, 2018, pp. 1–9.

[7] F. Argomedo *et al.*, "Model-based control of the magnetic flux profile in a tokamak plasma," in *49th IEEE Conference on Decision and Control (CDC)*, 2011.

[8] F. Felici and O. Sauter, "Non-linear model-based optimization of actuator trajectories for tokamak plasma profile control," *Plasma Physics and Controlled Fusion*, vol. 54, no. 2, p. 025002, 2012.

[9] M. Boyer, J. Barton, E. Schuster and others, "First-principles-driven model-based current profile control for the DIII-D tokamak via LQI optimal control," *Plasma Phys. Control. Fusion*, vol. 55, p. 105007, 2013.

[10] Y. Ou, T. Luce, E. Schuster, J. Ferron, M. Walker, C. Xu, and D. Humphreys, "Towards model-based current profile control at DIII-D," *Fusion Engineering and Design*, vol. 82, no. 5-14, pp. 1153–1160, Oct 2007.

[11] J. Barton, W. Shi, *et al.*, "Physics-based control-oriented modeling of the current density profile dynamics in high-performance tokamak plasmas," in *52nd IEEE International Conference on Decision and Control*, 2013.

[12] Y. Huang, B. Xiao, Z. Luo, Q. Yuan, X. Pei, and X. Yue, "Implementation of GPU parallel equilibrium reconstruction for plasma control in EAST," *Fusion Engineering and Design*, vol. 112, pp. 1019–1024, 2016.

[13] J. Wesson, *Tokamaks*. Oxford, UK: Clarendon Press, 1984.

[14] F. Hinton and R. Hazeltine, "Theory of plasma transport in toroidal confinement systems," *Rev. Mod. Phys.*, vol. 48, pp. 239–308, 1976.

[15] O. Sauter, C. Angioni, and Y. Lin-Liu, "Neoclassical conductivity and bootstrap current formulas for general axisymmetric equilibria and arbitrary collisionality regime," *Physics of Plasmas*, vol. 6, no. 7, pp. 2834–2839, 1999.

[16] ITER EDA *et al.*, "ITER Physics Basis Editors," *Nuclear Fusion*, vol. 39, no. 12, pp. 2201–2215, 1999.

[17] D. Naidu, *Optimal Control Systems*. CRC Press, 2002.